Supporting Information

Protective Layers Based on Carbon Paint to Yield High Quality Large-Area Molecular Junctions with Low Contact Resistance

Senthil Kumar Karuppannan [1], Esther Hui Lin Neoh[1], Ayelet Vilan[2,], and Christian A. Nijhuis[1,3*]*

[1]Department of Chemistry, National University of Singapore, 3 Science Drive 3, Singapore 117543, Singapore.

[2] Department of Chemical and Biological Physics, Weizmann Institute of Science, Rehovot, Israel 76100, Israel.

[3]Graphene Research Centre, National University of Singapore, 6 Science Drive 2, Singapore 117546, Singapore.

Tel.: (+65) 6516 2667

E-mail: chmnca@nus.edu.sg, ayelet.vilan@weizmann.ac.il

Experiment details

We purchased silicon wafers (100, p-type, 500 ± 25 μm) with one side polished from University Wafers (USA). Carbon conductive paint (Structure Probe Inc (SPI) Supplies # 05006-AB, 21 mL, Lot number 1220501) was purchased from SPI Supplies. The CP was diluted with freshly distilled isopropanol (VWR Chemicals; lot: 17C284030, purity > 99.7%) with 1:1 which is the solvent in the CP: isopropanol. Gold was purchased from Super Conductor Material, Inc (USA) with a purity of 99.999%. The 1H, 1H, 2H, 2H-perfluorooctyltrichlorosilane (FOTS), 40% ammonium fluoride solution (NH_4F) and all n-alkanethiols were purchased from Sigma-Aldrich with a purity of 98%, we purified the n-alkanethiols precursor before use by flask column chromatography followed by re-crystallization from ethanol (AR grade) following a previously reported procedure.[1]

Template stripped gold (Au^{TS}). We used a previously reported method to prepare the ultra-smooth patterned Au substrates.[1]

Atomic layer deposition (ALD). We deposited 35 nm of Al_2O_3 on Au substrate using Savannah ALD deposition chamber located within a glove box using a previously reported method.[2] Template stripping of the Au substrates from the silicon wafers was carried out inside a glove box (890-THC series) in an atmosphere of N_2 with 2.5 ppm of O_2 and 1.5 ppm of H_2O. The Au substrate was transferred into the ALD deposition chamber at 0.3 Torr, where 35 nm Al_2O_3 insulating layer was deposited using trimethylaluminum (pulse 60 s) and water (pulse 60 s) as precursors. The deposition temperature was kept at 95 ºC, 350 cycles were taken corresponding to the deposition of 35 nm Al_2O_3.

Electron beam lithography (EBL). We used EBL (Jeol JBX-6300FS EBL) lithography to pattern 10 µm diameter pores on Au/Al_2O_3 substrates. We used 495-PMMA A7 (MicroChem) co-polymer solution, which is spin coated at rate of 2000 rpm for 78 s and then pre-backed at 180 °C for 3 min, followed by a e-beam exposure and developed the pattern using 1:3 ratio of isopropanol and tetramethyl ammonium hydroxide developer, which serves as the mask to etch the Al_2O_3 layer.

Deep reactive ion etching (DRIE). We etched 10 nm holes of 10 µm diameter in Al_2O_3 using the oxford plasma pro cobra 100 deep RIE. We used C_4F_8 (17 sccm), SF_6 (70 sccm), and O_2 (5 sccm) gases for Al_2O_3 etching process. Pressure in DRIE chamber was maintained at 10 mTorr, and 10 nm Al_2O_3 was etched at 650 W inductively coupled plasma power for 6 min.

Alkanethiolate monolayers in micropore. Self-assembled monolayers of n-alkanethiolates were formed inside the micropores by first immersing the pores into 40% NH_4F solution for 2 min with continuous shaking of the substrate to expose the gold surface, followed by rinsing with ethanol, and then immersion into the n-alkanethiolate SAM solution in ethanol. The SAMs were formed overnight. Finally, the samples were rinsed with ethanol and blown dried with N_2 gas.

Atomic force microscopy (AFM) The AFM images were obtained by Bruker Dimension FastScan AFM with tapping mode tips (FASTSCAN-A). AFM software NanoScope Analysis (version 1.4) was used to analyses the AFM images.

Scanning electron microscopy (SEM). The SEM images were obtained using a microscope JEOL JM6400 equipped with a 40 kV microprobe. To measure the SEM image

of the CP films, we prepared the CP films on a Au^{TS} substrate, by application of three separate droplets on the Au^{TS} substrate spinning at 6000 rpm/s.

Ultraviolet photoelectron Spectroscopy (UPS). We determined the work function of the CP filim with Kratos AXIS Supra spectrometer. He (I) source (21.2eV with a 55 μm aperture) was used for UPS, and we used a 10 V bias for the secondary electron cut-off measurements. Throughout the measurements, the sample was under ultra-high vacuum ($\sim 10^{-9}$ mbar), room temperature and the analysis area was maintained at 0.7 × 0.3 mm^2. The work function Φ values were determined by linear extrapolation of the secondary electron cut-off to the base line.

X-ray photoelectron spectroscopy (XPS). We performed XPS for template stripped CP-film from the Au^{TS}-SAM surface using a Kratos AXIS Supra spectrometer with a monochromatic Al K-alpha source (1486.6 eV at 15 mA, 15 kV). The analysis area was 0.7 x 0.3 mm^2. A 3.1-volt bias was applied to the sample to neutralise charge build up on the sample surface. Individual core levels were measured with a pass energy of 20 eV. The XPS spectra were charge-corrected by characterizing the C 1*s* core level from adventitious carbon on the samples.

Profilometer. We used profilometer (Bruker DXT-12-0494) to measure the thickness of the CP film deposited on a glass substrate (see details in SI).

Deposition of the Au electrodes. The thermal evaporator (Shenyang Keyi, China) was used to evaporate gold (200 nm) at a rate of 0.5 Å/s (at a base pressure of 5×10^{-6} mbar) on Si/SiO_2 at room temperature. We used shadow mask to deposit patterned Au on a silicon substrate, with a 0.3 × 0.3 mm contact pad connected with 0.03 × 1.0 mm line.

Electrical measurements. We followed previously reported procedures for the data collection and analysis of the *J*(V) curves.[3] We recorded the I-*V* curves and performed current retention tests using the home-written code in LabView (Version 2010) and a Keithley 6430 sub-femtoamp remote source meter.

Normalized differential conductance (NDC) analysis. We used MatLab code and applying the NDC function (Eq. 5, main text) over parabolic approximation (Eq. 4, main text) to extract tunneling parameters. The *J*-*V* curves were re-casted in NDC plots after smoothing of the data using the spline-smoothing function of MatLab (factor = 0.9999) to reduce the noise.

Impedance spectroscopy. We performed impedance measurements as described previously.[4] Briefly, we measured impedance spectroscopy using a Solartron impedance analyzer (Solartron 1260A with 1296A dielectric interface) in reference mode with a standard 10 pF capacitor as the external reference. All the impedance measurements were repeated 3 – 5 times for each junction, this was repeated for three different junctions. The impedance measurements were conducted by applying an AC voltage of 30 mV at DC bias voltage of 0 V and the frequency was varied from 250 Hz to 1 MHz with 10 frequencies per decade.

Temperature dependent measurements. The *J* (V) measurements of the junctions as a function of temperature *T* were carried out in a probe station (Lakeshore CRX-VF) at a pressure of 1×10^{-5} bar as described elsewhere.[3] A code written in LabView (version 2010) was used to operate the source meter (Keithley, model 6430) was used to record the *J*(V) curves. The change of pressure from ambient to vacuum and solidification of the

bulk EGaIn at T = 220–240 K did not result in shorts, open circuits, or changed the electrical characteristics of the devices notably in any other notable way.

Section S1. To measure the thickness of the CP film, we prepared a patterned CP films on a glass substrate spin-coating CP on a glass substrate that was partially covered with Scotch tape. We removed the Scotch tape after spin-coating. The inset of Figure S2 shows a photograph of the glass surface with only one side coated with CP. Figure S2 shows the height profile (measured with a profilometer) of the edge of the CP film from which we determined the thickness of the film of ~1.0 μm. We determined the average size of the graphite flakes from SEM images obtained from diluted layers of the CP using different lot numbers to understand the batch-to-batch consistency of the CP product. Figure S3 shows the histograms of the graphite flake size distribution with Gaussian fits to these histograms for 3 different lot numbers. The Gaussian fit yields the Gaussian mean, along with the Gaussian standard deviation, of the size of the graphite flakes: 0.18 ± 0.02 μm for lot number 1220501 (Fig. S3A), 0.19 ± 0.01 μm for lot number 1230420 (Fig. S3B), and 0.20 ± 0.02 μm for lot number 1239429 (Fig. S3C). Thus, we confirm that the CP film is highly reproducible and does not depend on the lot number.

Figure S4 shows all the fabrication steps of the template-stripped carbon paint (CP^{TS}). We prepared a SAM of SC_{12} on Au^{TS} (Fig. S4A) using a previously reported method.[1] The SAMs were formed by immersion of the Au^{TS} substrate into the corresponding ethanoic solution of SC_{12} (Fig. S4B). The CP was deposited by spin-coating at 6000 rpm (Fig. S4C) followed by applied scotch tape support on the CP film (Fig. S4D). After applied scotch tape support, we applied small pressure on the tape using

cotton buds to make sure tape support properly stick to the CP film surface. Finally, the CP film with tape support striped from the Au^{TS}/SAM surface and then the CP^{TS} film used for AFM, and XPS characterization. To study the batch-to-bacth consistency of the CP^{TS} film, we measured topography of the CP surfaces with AFM for CP^{TS} films prepared from the three different batches (lot numbers, 1220501, 1230420, and 1239429); these results are summarized in Figure S5. Figure S6 shows the AFM images that were used to determine the area available for contact following the same procedure reported in ref [5]. Briefly, we estimated area available for the contact from digital analysis of a high resolution AFM image of a Au^{TS} and template stripped CP film, the available contact is the number of pixel within 0.2 nm from the top-most average plane of the digital image divided by the total number of pixels using Nanoscope analysis software.

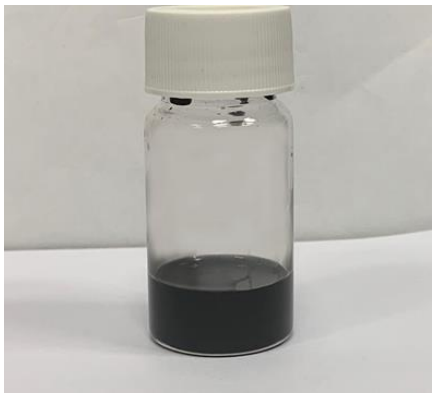

Figure S1. Optical photograph of an 8 week old suspension of diluted CP in isopropanol as used in our experiments to demonstrate the stability of the suspension: no sedimentation could be observed. According to the specifications of the manufacturer,[6] the concentrated CP has an indefinite shelf-life.

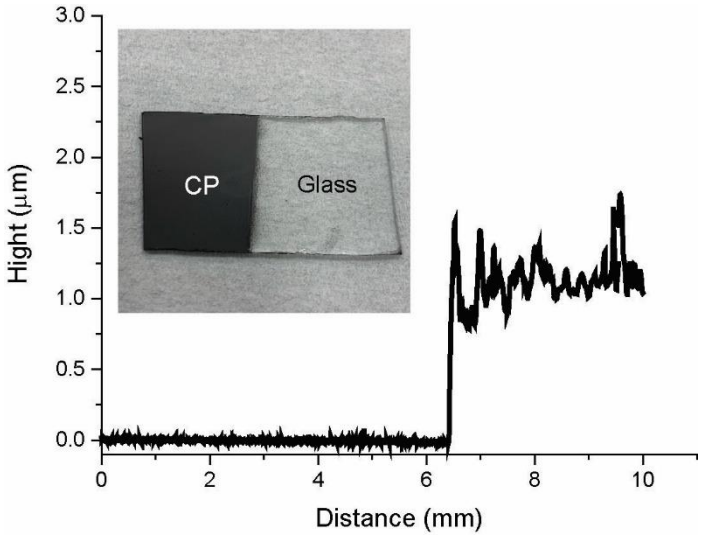

Figure S2. Height profile of carbon paint deposited by spin-coating on a glass substrate at 6000 rpm. Inset shows the optical image of the sample.

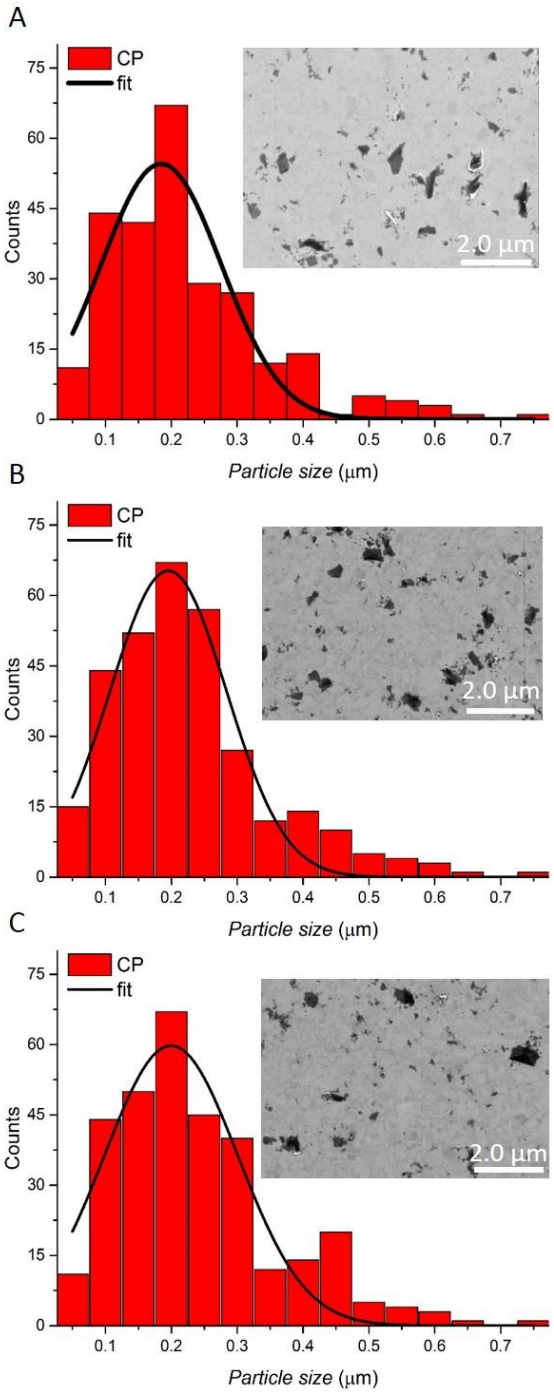

Figure S3. Histograms of the graphite flake size distribution determined with carbon paint obtained from 3 different lot numbers A) 1220501, B) 1230420, and C) 1239429, along with a Gaussian fit to these histograms. The inset shows respresentative SEM images used in our analysis.

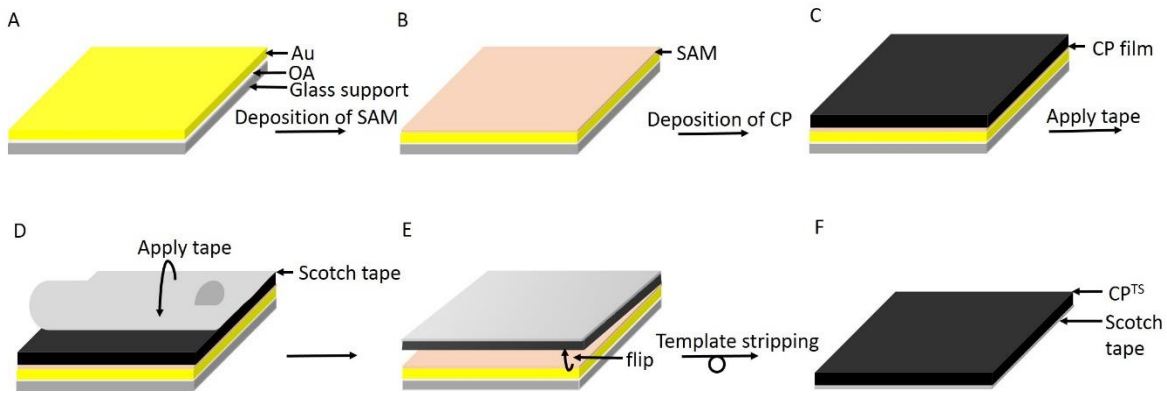

Figure S4. Schematic illustration of the fabrication of template-stripped carbon paint (CP^{TS}). A) Template stripped gold (Au^{TS}) surface, B) formation of the SAM, C) spin-coating of the CP layer, D) apply Scotch tape, E) peel off the Scotch tape with the CP film, and F) the CP^{TS} surface supported by the Scotch tape.

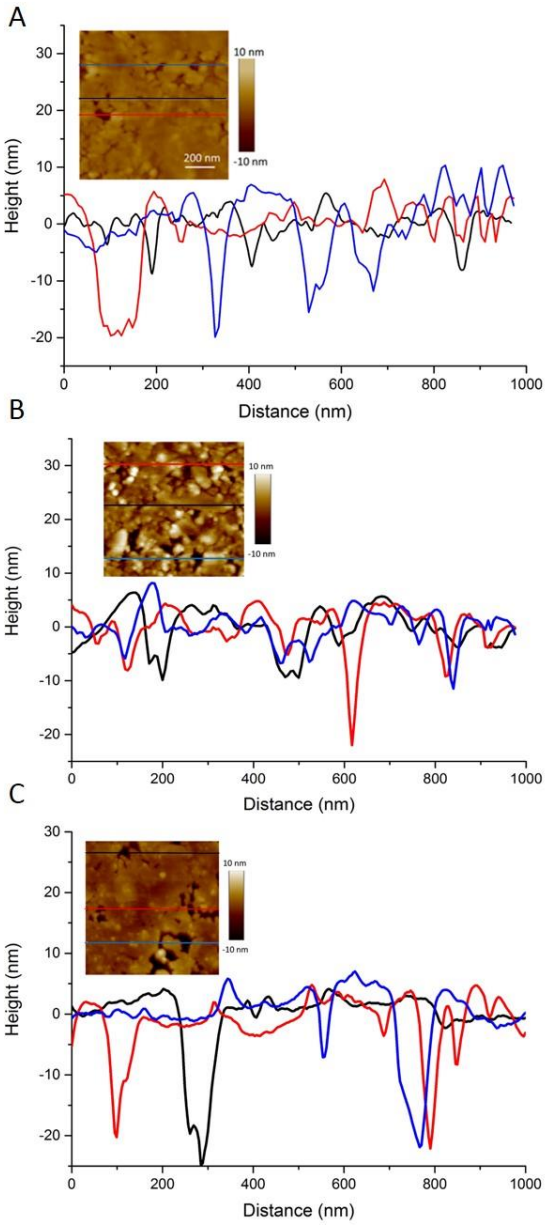

Figure S5. AFM line profiles recorded from template-stripped CP films prepared with CP with different lot number A) 1220501, B) 1230420, and C) 1239429, the inset shows the corresponding AFM image. The different line colors indicate the locations at which the line profiles were recorded.

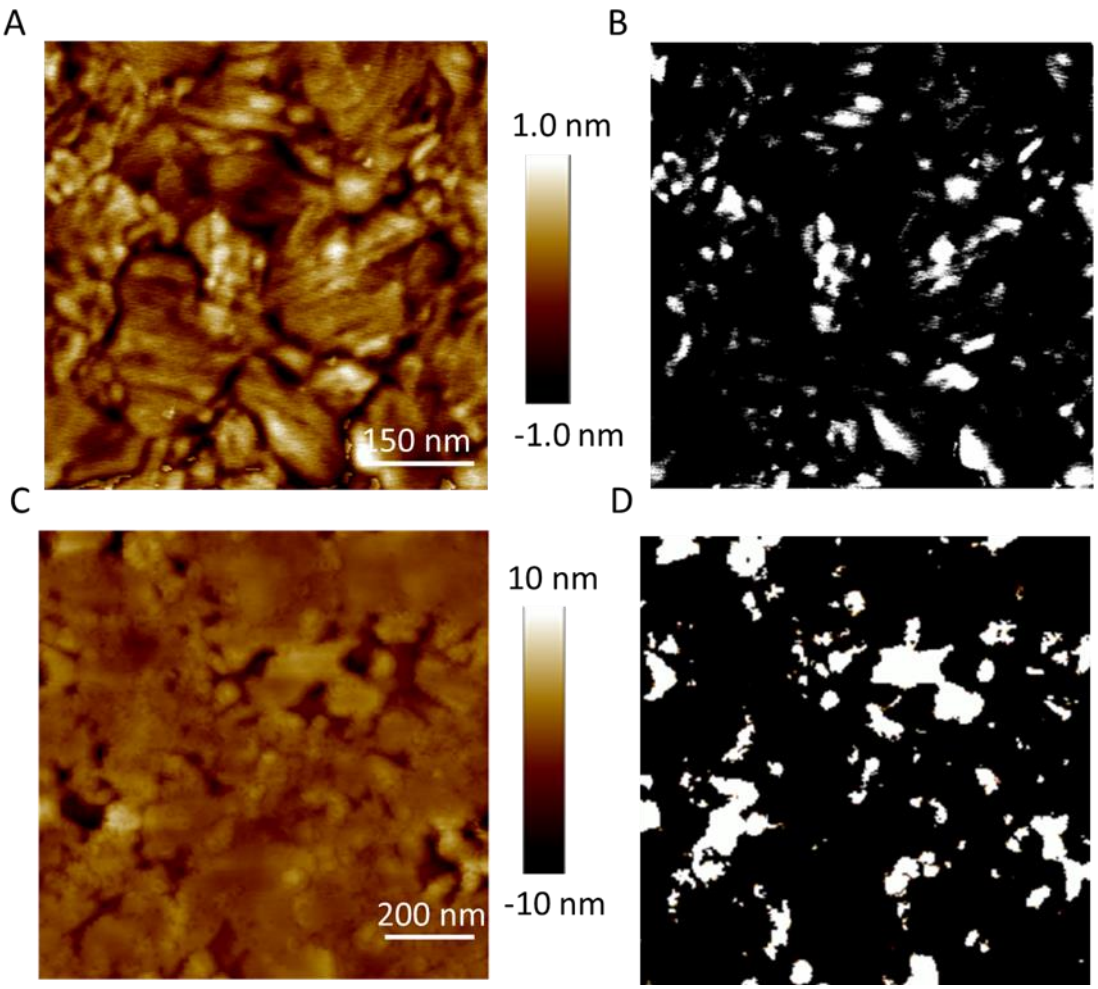

Figure S6. A) AFM image of Au^{TS}/SC_{10} inside the micropore (area of the image 0.6 × 0.6 μm^2), and B) surface area available for contact (white area) estimated from the nanoscope software analysis of the AFM image A. The surface area available for contact was estimated as the number of pixels within 0.2 nm from the top-most average plane of the image. C) AFM image of the CP layer (area of the image 1.0 × 1.0 μm^2), and D) surface area available for contact (white area) estimated from the nanoscope software analysis of the AFM image C.

Section S2. Figures S8 and S9 show the high resolution C 1*s* and O 1*s* XPS spectra of the CP films prepared using different lot numbers A-B) 1220501, C-D) 1230420, and E-F) 1239429 before (Fig. S8) and after (Fig. S9) cleaning with in situ Ar sputtering. Both C 1*s* XPS spectra show that the most dominant peak is at 284.3 eV (C=C), accompanied by additional peaks around 284.9 eV, 286.2 eV, 287.5 eV, and 288.7 eV, which correspond to the following carbon compounds, C-C, C-OH, =C-O and C=O. After cleaning, the solvent (C-OH) peak intensity was reduced, the peak at 288.7 eV was not observed. These observations indicate that most of the contaminations present on the as prepared surfaces originate for adventitious carbon. The high resolution O 1*s* XPS spectra before and after cleaning, both show a dominant peak at 532.4 eV corresponding to C-O, confirming the presence of the solvents. The additional peak at 533.4 eV corresponds to =C-O indicating the presence of physisorbed solvent or oxygen. Thus, the cleaned CP films contain small amounts of sp^3 carbon, and small amounts of oxygen may originate from the solvent, presence of chemi- and physisorbed water, CO_2 or oxygen[7], and small amounts of carbon-based impurities from the ambient environment introduced during the fabrication (e.g., spin coated) of the CP films. Other =C-O peaks at 286.2 eV due to physisorbed solvent or oxygen present in the graphite film. Thus, the presence of oxygen signal after cleaning indicate that the oxides of pristine graphite are often observed due to the solvent, or physisorbed water or oxygen, or carbon oxides, introduced during the preparation of the CP films (e.g., during spin coating in ambient conditions).

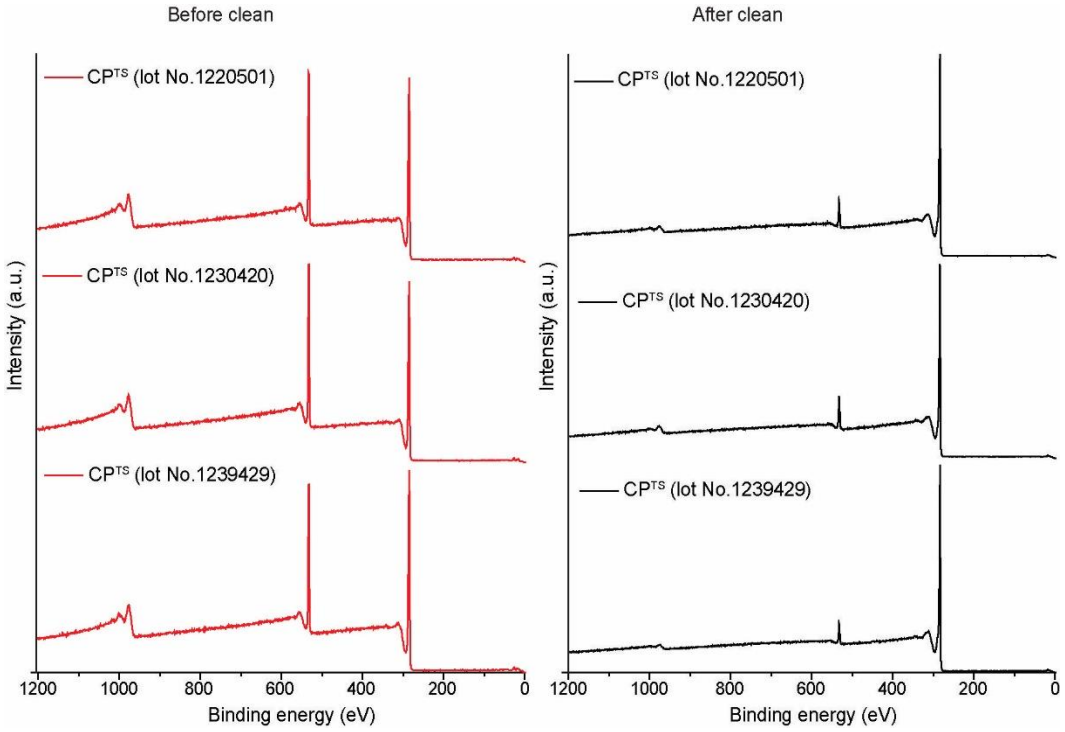

Figure S7. The XPS survey spectra of the template-stripped CP film prepared using a different lot number before (red line) and after (black line) cleaning.

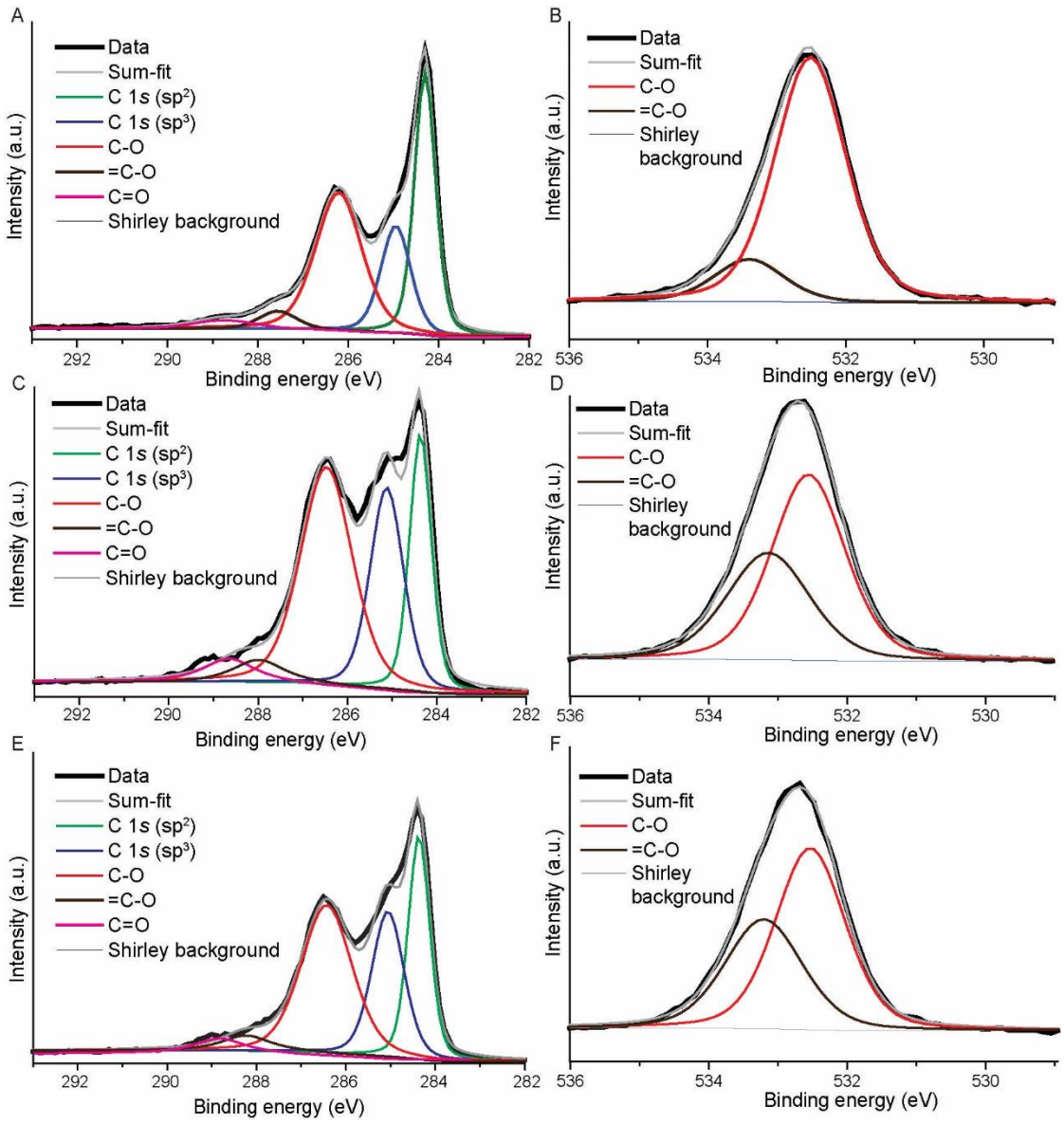

Figure S8. The XPS spectra of C 1*s* (A, C and E), and O 1*s* (B, D, and F) for the template-stripped CP film prepared using a different lot number A-B) 1220501, C-D) 1230420, and E-F) 1239429 before cleaning of the CP film.

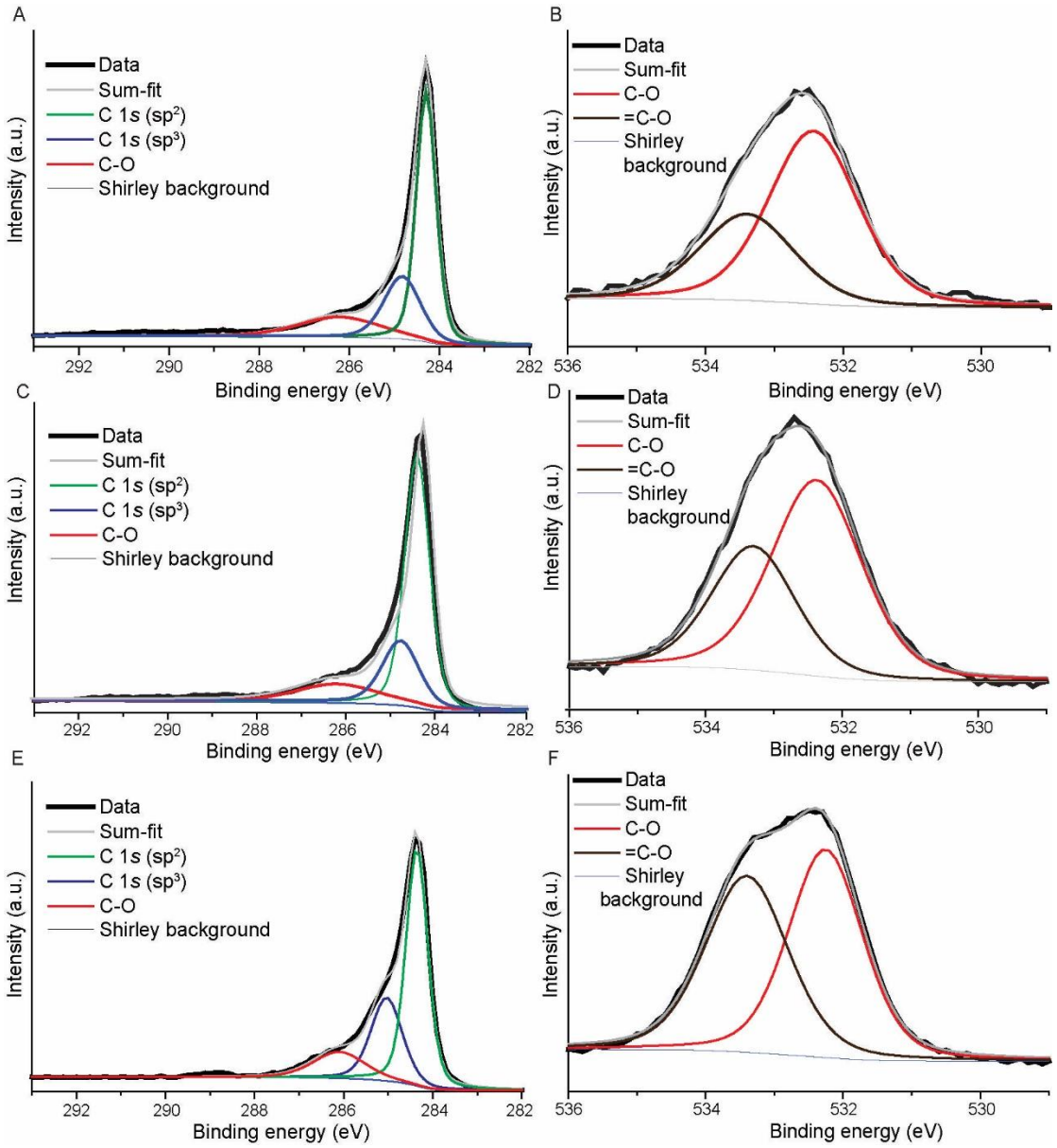

Figure S9. The XPS spectra of C 1*s* (A, C and E), and O 1*s* (B, D, and F) for the template-stripped CP film prepared using a different lot number A-B) 1220501, C-D) 1230420, and E-F) 1239429 after cleaning of the CP film.

Section 3. Vertical resistance of the CP film. To determine the vertical resistance of the CP film, we spin-coated ~1.0 μm thick CP film on a Au^{TS} substrate. Next, we deposited 100 nm thick Au contact pads with a dimension of 300 × 300 μm by using shadow mask

deposition after which the excess CP was removed with oxygen plasma etching. We used four-wire (Kelvin) method[8] (Fig. S10B) to measure vertical resistance of the CP film to reduce the effect of the probe contact resistance which is usually present in standard two terminal measurements. Here, the resistance was measured with a sourcing current using from Keighley 6221 source meter (applied constant current was 1.0 µA) and the voltage using a Keighley nanovoltmeter 2182A. The vertical resistance of the CP layer is 0.012 Ω (resistivity = ~0.10 Ω cm).

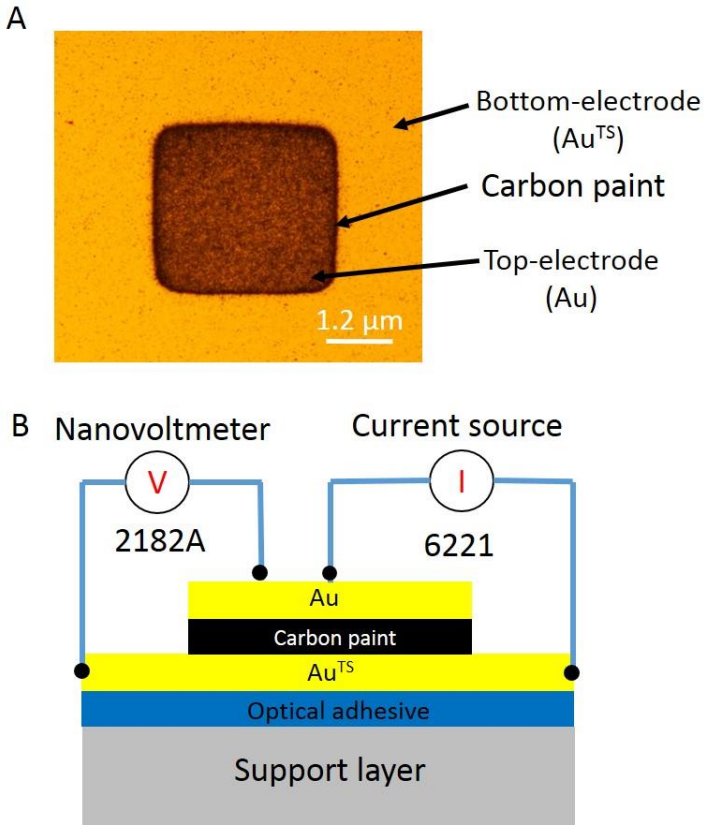

Figure S10. A) Optical microscopy image of the Au^{TS}//CP//Au junction, and B) a schematic of the four-wire measurement used to estimate resistivity of the junctions.

Section S4. **Statistical data analysis**. We recorded statistically large number of data (see Table S1) for the Au^{TS}-SC_n//CP//Au junctions. We followed the procedure for statistical analysis of the junction data as reported before.[9] We plotted the value of $\log_{10}|J|$ at given bias voltage (Figure S11) in histograms and fitted Gaussians to these histograms to obtain the Gaussian log-standard deviation ($\sigma_{\log G}$) and the Gaussian log-mean of the value of J, $<\log_{10}|J|>_G$, for each applied voltage; this was repeated for the various lengths of alkanthiolate SAMs. These data were used to construct the $<\log_{10}|J|>_G$ *vs.* V curves shown in the main text.

Table S1. Statistical analysis of J(V) measurements of Au^{TS}-SC_n//CP//Au junctions

SAMs	No of junctions	No of working junctions	Yield (%)[a]	Total Traces[b]	$\sigma_{\log G}$
SC_4	66	60	90	800	0.25
SC_6	102	80	78	910	0.45
SC_8	150	110	73	1200	0.25
SC_{10}	110	63	58	970	0.32
SC_{12}	121	92	76	1240	0.35
SC_{14}	78	58	74	780	0.36

[a] The yield of working junctions is defined as a percentage value of working junctions (junctions that were not open circuits, none of the junctions shorted) divided by a total number of junctions.

[b] The total number of J(V) traces are 10-20 scans for each stable junction.

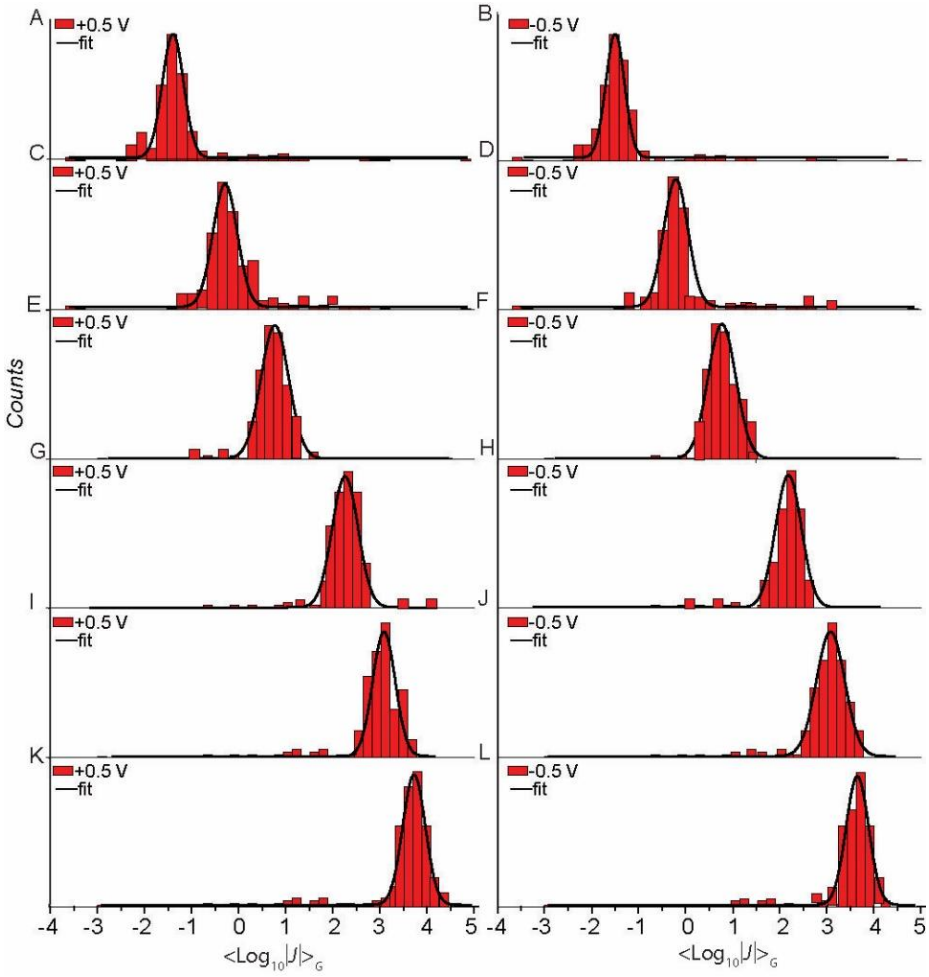

Figure S11. Histograms of $<\log_{10}|J|>_G$ obtained from Au^{TS}-SC_n//CP//Au junctions measured at ± 0.5 V for A-B) n = 14, C-D) n = 12, E-F) n = 10, G-H) n = 8, I-J) n = 6, and K-L) n = 4, samples.

Section S5. **Extraction of transport parameters**. We used all *J*(V) traces obtained from Au^{TS}-SC_n//CP//Au junctions with n = 4-14 (even numbers only) and then we extracted the transport parameters with NDC analysis as reported before.[2,10,11] The extracted transport parameters from the NDC analysis are plotted in Fig. 5 along with the standard deviations. Below are the histograms of $<\log_{10}|J|>_G$, heat maps of the NDC plots, and the histograms

of the extracted transport parameters. The *J*(V) curves on a linear scale are given in Fig. S16. Fig. S17 summarizes the possible potential profile of the junctions.

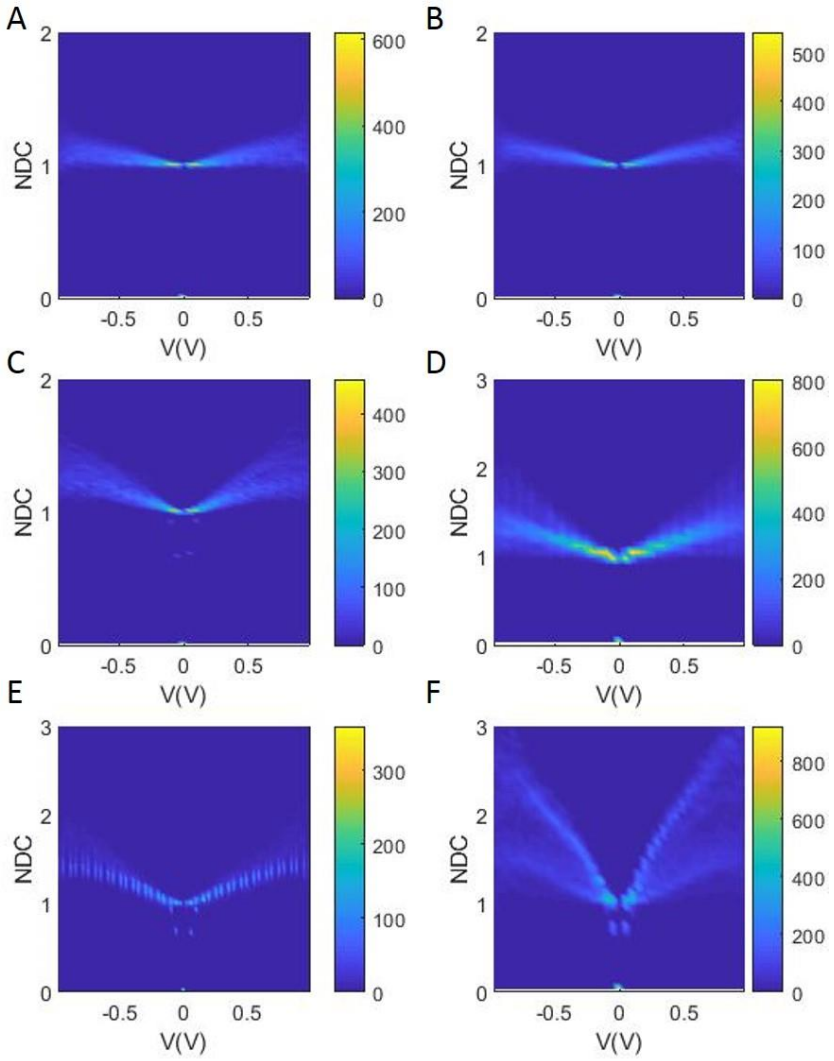

Figure S12. Heat maps of NDC *vs. V* (V) of Au^{TS}-SC_n//CP//Au junctions with A) n = 4, B) 6, C) 8, D) n = 10, E) 12, and F) 14, based on micropores with a diameter of 10 μm.

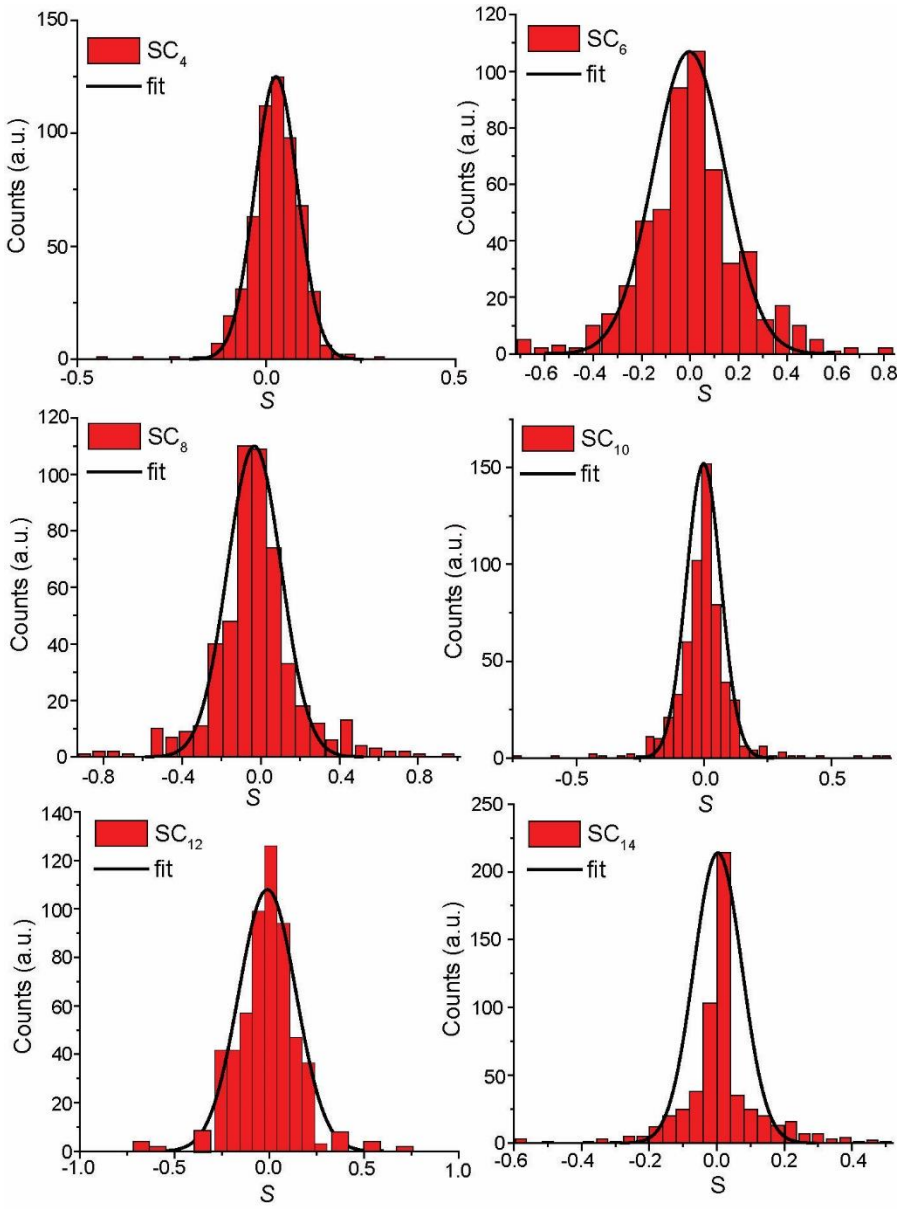

Figure S13. Histograms of asymmetric factor (*S*) obtained from NDC analysis of Au^{TS}-SC_n//CP//Au junctions with n = 4-14.

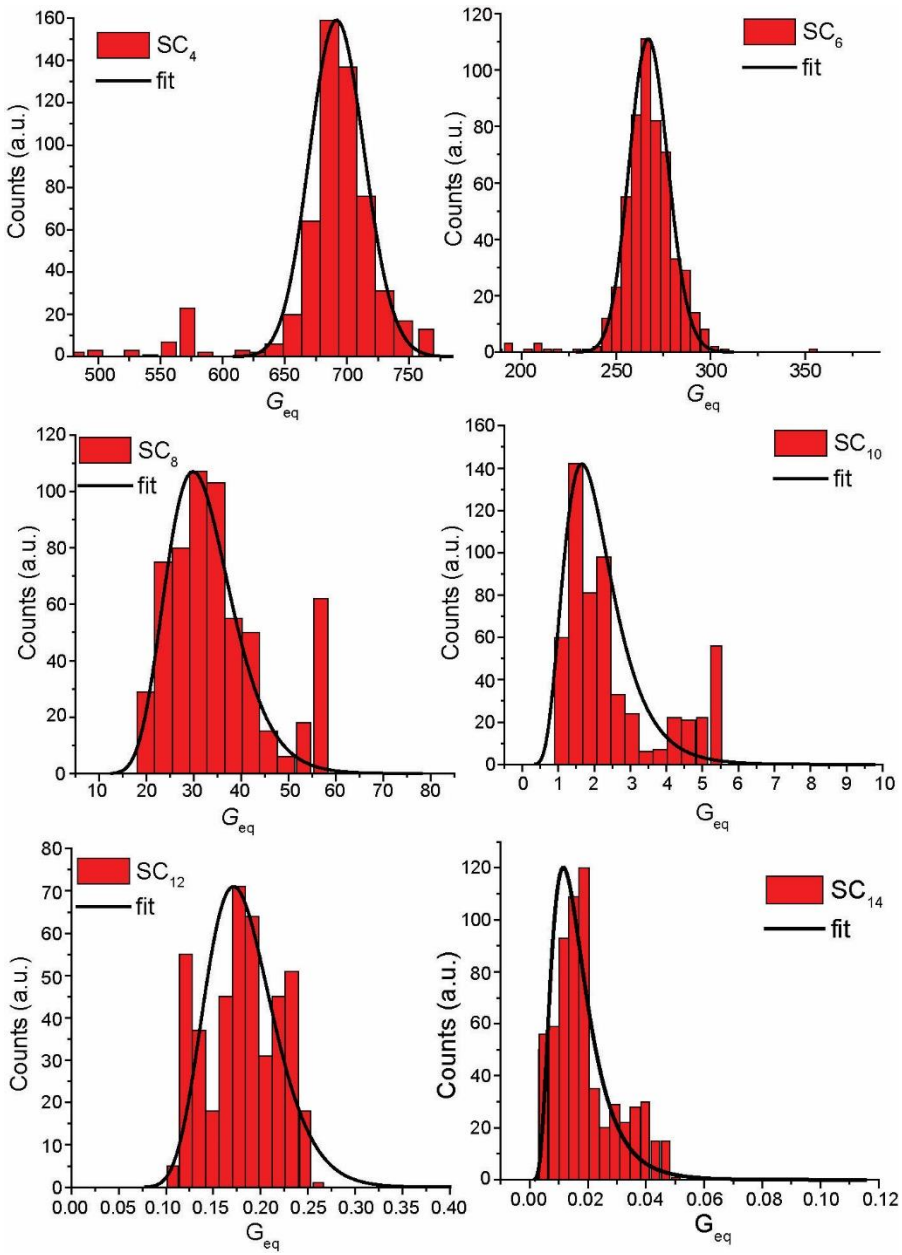

Figure S14. Histograms of equivalent conductance obtained from the NDC analysis of Au^{TS}-SC_n//CP//Au junctions with n = 4-14.

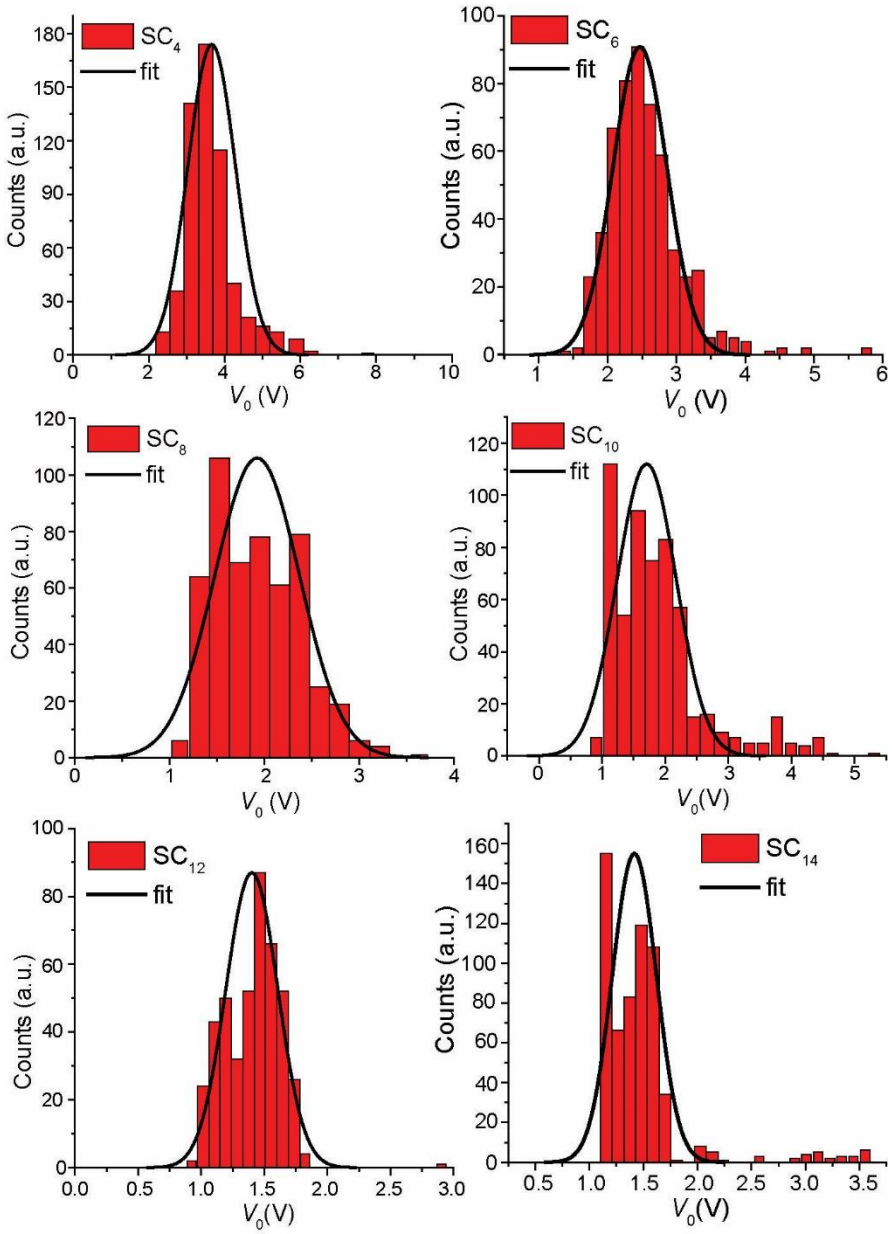

Figure S15. Histograms of parameter (V_0) obtained from the NDC analysis of Au^{TS}-SC_n//CP//Au junctions with n = 4-14.

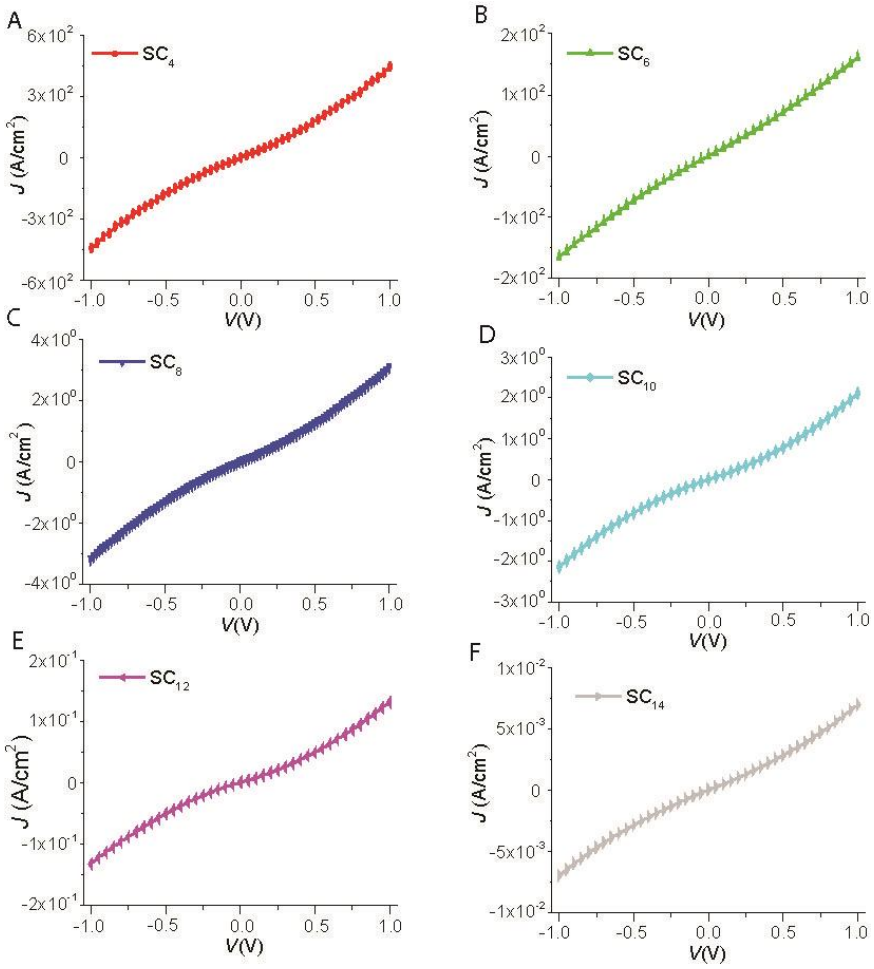

Figure S16. The *J vs. V* (V) of Au^{TS}-SC_n//CP//Au junctions with A) n = 4, B) 6, C) 8, D) n = 10, E) 12, and F) 14, based on micropores with a diameter of 10 μm.

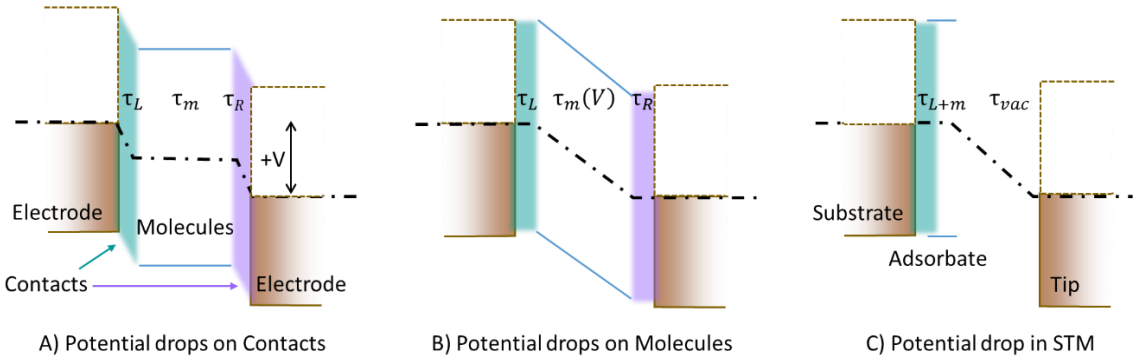

Figure S17: a schematic illustration of different voltage partitions in common molecular junctions, showing A) a flat barrier; B) a trapezoidal barrier and C) a tunneling gap as in STM experiment. Bluish-stripped area marks the molecular body while shaded green and purple are the poorly-defined interface regions. The left electrode (shaded brown) is eV higher in energy than the right electrode; this potential step falls either on the interfaces (A), on the molecular body (B) or on a tiny vacuum gap (C). τ_i marks the different contributions to the net transmission probability; common transport models generally view τ_i as independent of the applied voltage, accept for the trapezoidal barrier (B), where the molecule is highly distorted by the huge electric field. Scenario C may partly apply for highly rough top-electrode that cannot produce an intimate contact.

Section 6. **Impedance data analysis**

The impedance data were validated (*i.e.*, to establish the junctions were in thermodynamic equilibrium and stable during the measurements, and that higher harmonics were not important) with Kramers−Kronig (KK) transformations (see Section S7 and 8, Fig. S18 and 19) and Table S2 lists the values of χ^2_{KK} and the values of χ^2_{fit} which are similar to χ^2_{KK}.

Figure S20 shows the Nyquist plots for the three different junctions. The phase spectrum shows one peak (Figure 6B main text) and the Nyquist plot shows the presence of one semicircle (Figure S20), which indicates the presence of one capacitance in the junctions.

The CPE contains an additional constant (n_e) in the exponent which is used to account for non-ideal capacitive behavior due to defects in the electrodes (induced by,

e.g., surface roughness): n_e = 1 represents an ideal capacitor, but here we used slightly smaller values in the range of n_e = 0.98 - 0.99 to obtain good fits (Section 7). The parallel plate equation is given by

$$C_{SAM} = \varepsilon_0 \varepsilon_{SAM} A_{geo}/d \qquad \text{(S1)}$$

where ε_0 is the permittivity of the free space, ε_{SAM} is the dielectric constant of the n-alkanethiolate SAM, and A_{geo} is the geometrical area of the junctions. The intercept of the fit with Eq. S1 (Fig. S21) and the y-axis yields the stray capacitance of 6.19 μF/cm^2, which close to the stray capacitance estimated from the equation S1 (see for details Section S9). The AlO_x layer is very thin and we have shown before that Au directly deposited on this thin layer results in pinholes,[2] but the impedance results indicate that the CP does not penetrate the AlO_x layer. We have confirmed this conclusion by measuring the *J*(V) curve of a Au^{TS}//AlO_x//CP//Au junction across which we could not measure a current within the detection limit of our electrometer (see Section S10, Fig. S22). Thus, the SAM inside the micropore dominates the charge transport process across the junctions. From the capacitance of the SAM, C_{SAM}, we extracted a relative dielectric constant of 3.1 ± 0.4 which is similar to previously reported values for n-alkanthiolate SAMs in other types of junctions.[12–14] and the results confirm that stray capacitances are insignificant (see Section S10 for measurements on Au^{TS}//AlO_x//CP/Au junctions).

Section S7. Kramer-Kronig (KK) analysis. Figure S18 shows the KK-plots of the Au^{TS}-SC_n//CP//Au junctions. No trends are visible, therefore we conclude that the data are linear and that the junctions did not change during the measurements. The measured impedance data are of reasonable quality (Table S2) with acceptable signal-to-noise

ratios (although noise levels were in general 2-3% in the low-frequency regime and increased to roughly 15% in the high-frequency regime).

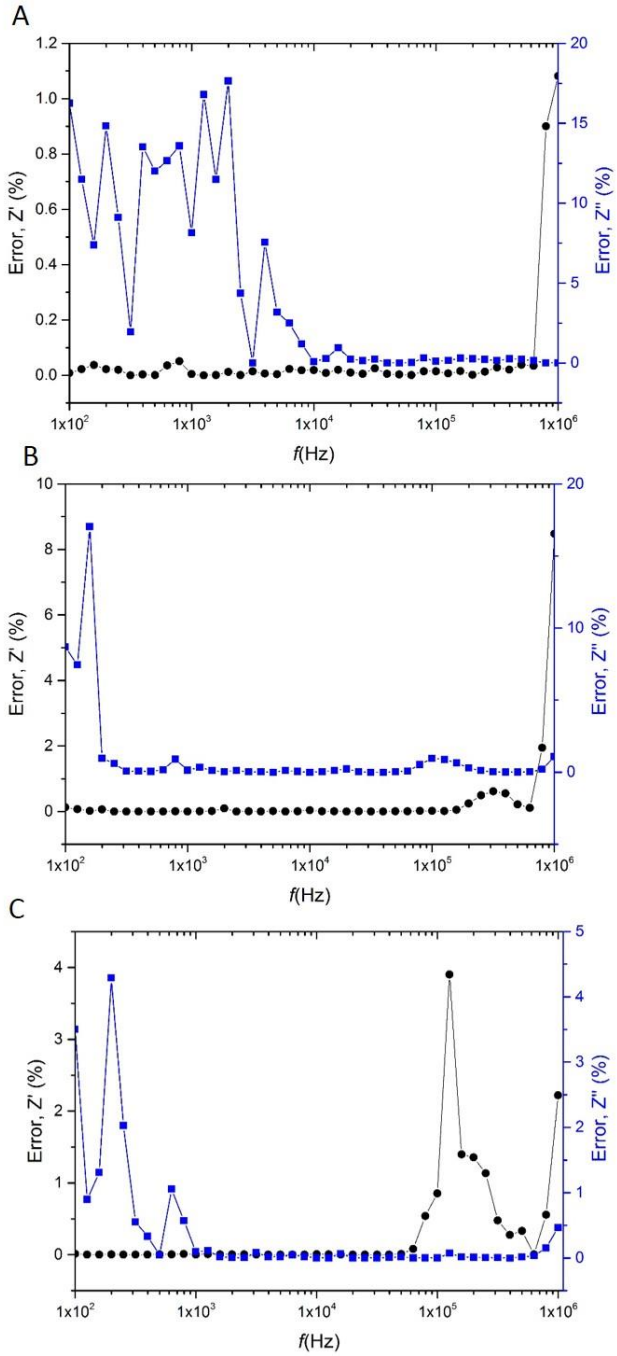

Figure S18. Kramers-Kronig residual plots for Au^{TS}-SC_n//CP//Au junctions with n = (A) 10, (B) 12, and (C) 14.

Section S8. Residual plots. Figure S19 shows the residual plots for nonlinear least square fitting of the impedance data to the equivalent circuit shown in Figure 6A as described in the main text. The values of χ^2_{Fit} are summarized in Table S2. The χ^2_{Fit} values are close to the χ^2_{KK} values.

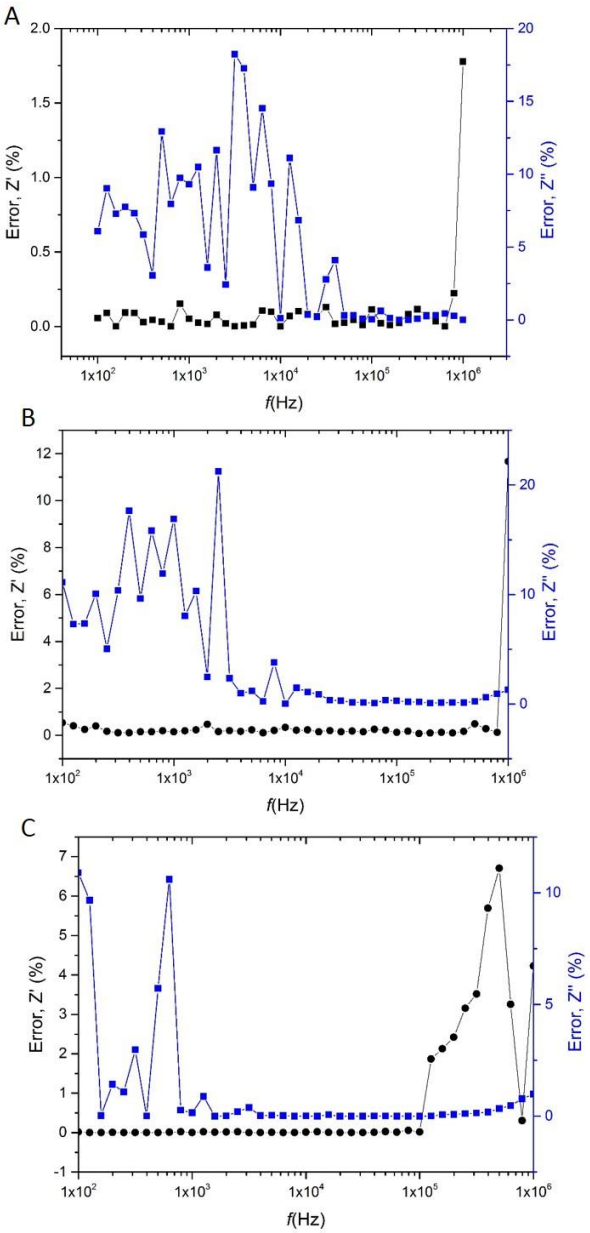

Figure S19. Residual plots for the equivalent circuit model fitting to the average impedance data of Au^{TS}-SC_n//CP//Au junctions with n = (A) 10, (B) 12, and (C) 14.

Table S2. The χ^2 values from KK-fit and fitting to the equivalent circuit

Tunnel junction	χ^2 KK	χ^2 fits
Au^{TS}-SC_{10}//CP//Au	0.0057	0.0076
Au^{TS}-SC_{12}//CP//Au	0.0075	0.0085
Au^{TS}-SC_{1}//CP//Au	0.0029	0.0042

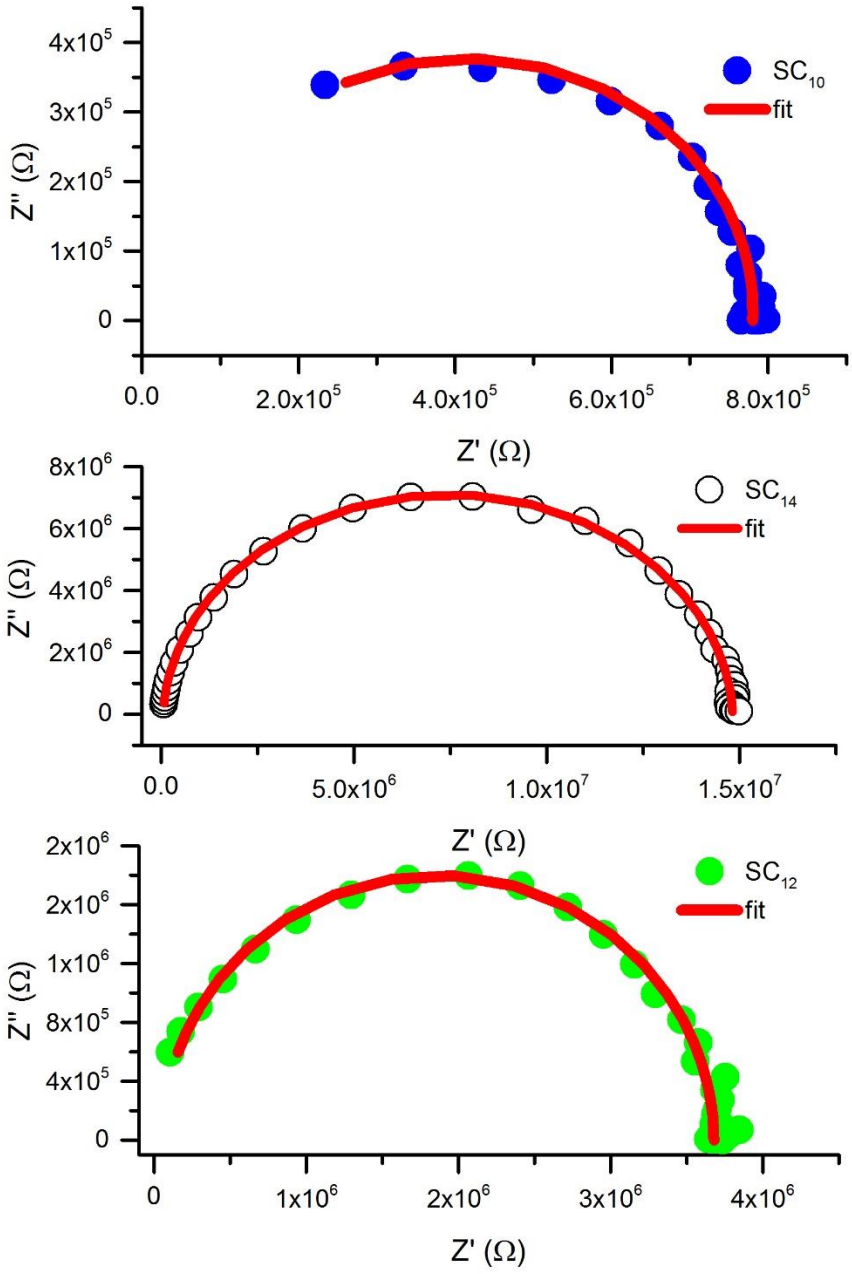

Figure S20. Nyquist plots and fits (solid lines) to the equivalent circuit for SC_{10}, SC_{12}, and SC_{14}. The data presented here are an average of three sets of measurements.

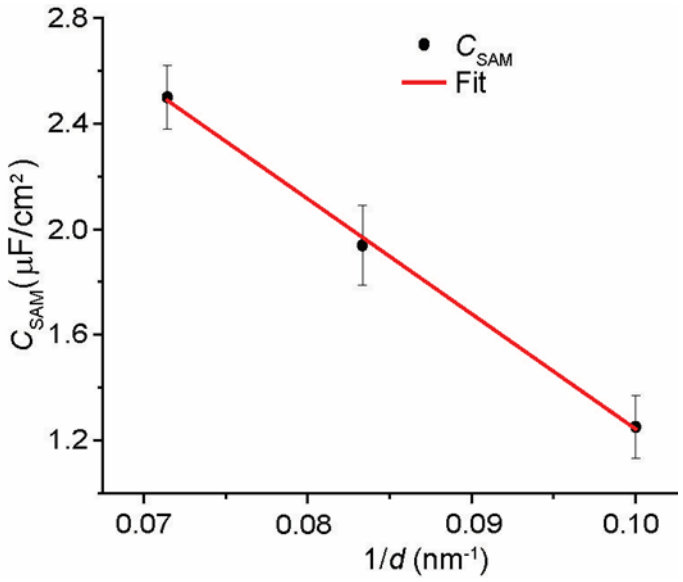

Figure S21. Capacitance of SAM (C_{SAM}) *vs.* SC_n, the red line is a fit to the Eq. S1. The error bars represent the log-standard deviations obtained from three independent measurements.

Section S9. Stray capacitance. To confirm C_{stray} can be ignored, we used Eq. S2 to estimate the value of C_{stray}

$$C_{stray} = \frac{\varepsilon_0 \varepsilon_r}{d} \qquad \text{S2}$$

where, d, ε_0, and ε_r, are the contact area of Au^{TS}//AlO_x//CP/Au junction, the distance between two electrodes of 10 nm, ε_0 is the permittivity of the free space, and ε_r the relative dielectric constant of insulator (9 for AlO_x), respectively.[1] This estimation yields C_{stray} = 0.79 μF/cm^2. This estimation confirms that C_{stray} is not important in our devices.

Section S10. To confirm that the leakage current across the 10 nm AlO_x is not important for our large area junctions, we deposited 10 nm AlO_x on a patterned Au^{TS} substrate

using ALD and then spin-coated a ~1.0 μm thick CP film on the Au^{TS}/AlO_x substrate. Next, we deposited 100 nm Au with a dimension of 50 × 1000 μm through a shadow mask after which the excess the CP was removed with oxygen plasma etching. Figure S21 shows the *J*(V) curve for the $Au^{TS}//AlO_x//CP//Au$ junction, we did not observe a significant current across the junction, which confirms that the leakage current across the 10 nm AlO_x is insignificant.

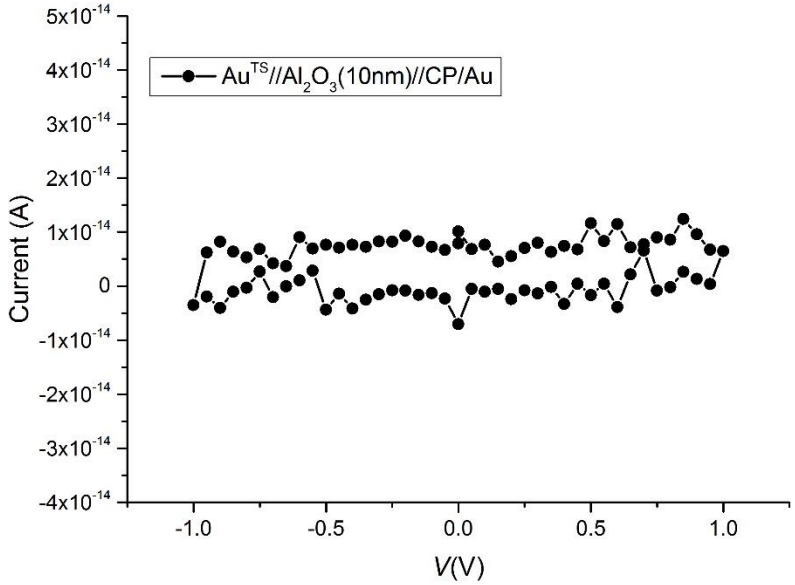

Figure S22. The *I*(V) characteristics of a Au^{TS}//10 nm AlO_x //CP/Au junction.

References

(1) Yuan, L.; Jiang, L.; Zhang, B.; Nijhuis, C. A. Dependency of the Tunneling Decay Coefficient in Molecular Tunneling Junctions on the Topography of the Bottom Electrodes. *Angew. Chemie - Int. Ed.* **2014**, *53*, 3377–3381.

(2) Karuppannan, S. K.; Hongting, H.; Troadec, C.; Vilan, A.; Nijhuis, C. A. Ultrasmooth and Photoresist-Free Micropore-Based EGaIn Molecular Junctions: Fabrication and How Roughness Determines Voltage Response. *Adv. Funct. Mater.* **2019**, *29*, 1904452.

(3) Wan, A.; Jiang, L.; Sangeeth, C. S. S.; Nijhuis, C. A. Reversible Soft Top-Contacts to Yield Molecular Junctions with Precise and Reproducible Electrical Characteristics. *Adv. Funct. Mater.* **2014**, *24*, 4442–4456.

(4) Suchand Sangeeth, C. S.; Wan, A.; Nijhuis, C. A. Probing the Nature and Resistance of the Molecule–Electrode Contact in SAM-Based Junctions. *Nanoscale* **2015**, *7*, 12061–12067.

(5) Simeone, F. C.; Yoon, H. J.; Thuo, M. M.; Barber, J. R.; Smith, B.; Whitesides, G. M. Defining the Value of Injection Current and Effective Electrical Contact Area for EGaIn-Based Molecular Tunneling Junctions. *J. Am. Chem. Soc.* **2013**, *135*, 18131–18144.

(6) SPI Supplies Division Structure Probe, Inc. 206 GARFIELD AVE., WEST CHESTER, PA 19380 https://www.2spi.com/.

(7) Susi, T.; Pichler, T.; Ayala, P. X-Ray Photoelectron Spectroscopy of Graphitic Carbon Nanomaterials Doped with Heteroatoms. *Beilstein J. Nanotechnol.* **2015**,

6, 177–192.

(8) P., A.; C., Z.; K., P. Hafnium-Based High-k Gate Dielectrics. In *Advances in Solid State Circuit Technologies*; InTech, 2010; pp 333–350.

(9) Reus, W. F.; Nijhuis, C. A.; Barber, J. R.; Thuo, M. M.; Tricard, S.; Whitesides, G. M. Statistical Tools for Analyzing Measurements of Charge Transport. *J. Phys. Chem. C* **2012**, *116*, 6714–6733.

(10) Vilan, A. Analyzing Molecular Current-Voltage Characteristics with the Simmons Tunneling Model: Scaling and Linearization. *J. Phys. Chem. C* **2007**, *111*, 4431–4444.

(11) Vilan, A.; Cahen, D.; Kraisler, E. Rethinking Transition Voltage Spectroscopy within a Generic Taylor Expansion View. *ACS Nano* **2013**, *7*, 695–706.

(12) Akkerman, H. B.; Naber, R. C. G.; Jongbloed, B.; van Hal, P. A.; Blom, P. W. M.; de Leeuw, D. M.; de Boer, B. Electron Tunneling through Alkanedithiol Self-Assembled Monolayers in Large-Area Molecular Junctions. *Proc. Natl. Acad. Sci.* **2007**, *104*, 11161–11166.

(13) Rampi, M. A.; Schueller, O. J. A.; Whitesides, G. M. Alkanethiol Self-Assembled Monolayers as the Dielectric of Capacitors with Nanoscale Thickness. *Appl. Phys. Lett.* **1998**, *72*, 1781–1783.

(14) Jiang, L.; Sangeeth, C. S. S.; Yuan, L.; Thompson, D.; Nijhuis, C. A. One-Nanometer Thin Monolayers Remove the Deleterious Effect of Substrate Defects in Molecular Tunnel Junctions. *Nano Lett.* **2015**, *15*, 6643–6649.